


Cite this: *RSC Adv.*, 2022, 12, 34760

# MoO<sub>2</sub> nanosheets anchored with Co nanoparticles as a bifunctional electrocatalytic platform for overall water splitting†

Lu Xia,<sup>a</sup> Yanjun Li,<sup>a</sup> Hao Song,<sup>bc</sup> Xingxing Li,<sup>b</sup> Wenjie Gong,<sup>a</sup> Xinyu Jiang,<sup>a</sup> Mehran Javanbakht,<sup>id d</sup> Xuming Zhang,<sup>id b</sup> Biao Gao<sup>id \*b</sup> and Paul K. Chu<sup>id \*c</sup>

Electrochemical water splitting is one of the potential commercial techniques to produce clean hydrogen energy because of the high efficiency and environmental friendliness. However, development of low-cost bifunctional electrocatalysts that can replace Pt-based catalysts for the hydrogen evolution reaction (HER) and oxygen evolution reaction (OER) is challenging. Herein, Co nanoparticles (NPs) are anchored on MoO<sub>2</sub> nanosheets (Co/MoO<sub>2</sub>) by thermal reduction of the CoMoO<sub>4</sub> nanosheet array in Ar/H<sub>2</sub>. The uniformly distributed Co NPs improve the electron transfer capability and modulate the surface states of the MoO<sub>2</sub> nanosheets to enhance hydrogen desorption and HER kinetics. Moreover, the Co/MoO<sub>2</sub> composite is beneficial to the interfacial structure and the MoO<sub>2</sub> nanosheets prevent aggregation of Co NPs to improve the intrinsic OER characteristics in the alkaline electrolyte. As a result, the Co/MoO<sub>2</sub> electrocatalyst shows low HER and OER overpotentials of 178 and 318 mV at a current density of 10 mA cm<sup>-2</sup> in 1 M KOH. The electrolytic cell consisting of the bifunctional Co/MoO<sub>2</sub> electrodes shows a small voltage of 1.72 V for a current density of 10 mA cm<sup>-2</sup> in overall water splitting.

Received 28th September 2022

Accepted 2nd November 2022

DOI: 10.1039/d2ra06117a

rsc.li/rsc-advances

## 1 Introduction

Hydrogen (H<sub>2</sub>) energy is one of the candidates to replace fossil fuels because of its environmental friendliness, small weight, and high energy density. Electrocatalytic water splitting is one of the preferred means to produce H<sub>2</sub> and O<sub>2</sub>.<sup>1–3</sup> Water splitting includes the hydrogen evolution reaction (HER) and oxygen evolution reaction (OER) that require proper catalysts to boost efficiency. Some noble metals such as Pt and Pd possess high electrocatalytic activity and low overpotentials in HER and noble metal oxide catalysts such as RuO<sub>2</sub> and IrO<sub>2</sub> are common catalysts for OER. However, the high cost and natural scarcity of these noble materials hamper large-scale commercial application.<sup>4–6</sup> HER can take place in both acid and base media but OER is undesirable in acidic electrolytes. Hence, preparation of efficient bifunctional noble-metal-free electrocatalysis

for both HER and OER in alkaline media is challenging albeit of prime importance.

Owing to the high abundance and low cost, rutile molybdenum dioxide (MoO<sub>2</sub>) is garnered interest in water splitting<sup>7</sup> and nanostructures such as nanoparticles,<sup>8</sup> nanobelts,<sup>9</sup> nanosheets,<sup>10</sup> nanoflowers,<sup>11</sup> nanowires<sup>12</sup> and hierarchical nanoarrays<sup>13</sup> have been developed to improve H<sub>2</sub> evolution by increasing the surface area and increasing the reaction sites. Chen *et al.* have demonstrated that the Mo atom in MoO<sub>2</sub> is a high d-band center because of expansion of the Mo lattice upon incorporation of oxygen, resulting in unfavorable H<sub>2</sub> kinetics and poor H<sub>2</sub> evolution activity on MoO<sub>2</sub>.<sup>14</sup> Introducing transition metals to fill the empty d orbitals of Mo can weaken the Mo–H binding energy and improve the hydrogen evolution efficiency.<sup>15–18</sup> Zhao *et al.* have constructed a CoP and MoO<sub>2</sub> heterostructure to coordinate interface electrons and accelerate dissociation of water and adsorption of hydrogen.<sup>19</sup> Recent research activities have focused on improving the HER performance of MoO<sub>2</sub> catalysts but the OER characteristics have not been studied extensively.

Herein, MoO<sub>2</sub> nanosheets are anchored with Co nanoparticles (Co/MoO<sub>2</sub>) to serve as bifunctional electrocatalysts for both HER and OER by reducing CoMoO<sub>4</sub> grafted on a carbon cloth in the Ar/H<sub>2</sub> atmosphere. In this process, CoMoO<sub>4</sub> is separated *in situ* to form the Co/MoO<sub>2</sub> heterojunction with abundant Co and MoO<sub>2</sub> interface consequently improving the HER and OER properties simultaneously, as demonstrated by low overpotentials of 178 mV and 318 mV to achieve a current

<sup>a</sup>The College of Resources and Environment Engineering and Hubei Key Laboratory for Efficient Utilization and Agglomeration of Metallurgic Mineral Resources, Wuhan University of Science and Technology, Wuhan 430081, China

<sup>b</sup>The State Key Laboratory of Refractories and Metallurgy and Institute of Advanced Materials and Nanotechnology, Wuhan University of Science and Technology, Wuhan 430081, China. E-mail: gaobiao@wust.edu.cn

<sup>c</sup>Department of Physics, Department of Materials Science and Engineering, Department of Biomedical Engineering, City University of Hong Kong, Tat Chee Avenue, Kowloon, Hong Kong, China. E-mail: paul.chu@cityu.edu.hk

<sup>d</sup>Renewable Energy Research Center, Amirkabir University of Technology, Tehran, Iran

† Electronic supplementary information (ESI) available. See DOI: <https://doi.org/10.1039/d2ra06117a>



density of  $10 \text{ mA cm}^{-2}$  together with small Tafel slopes of  $102.6 \text{ mV dec}^{-1}$  and  $93.9 \text{ mV dec}^{-1}$  in HER and OER in 1 M KOH, respectively. The electrolytic cell assembled with the bifunctional Co/MoO<sub>2</sub> electrocatalyst shows a low overall water splitting voltage of 1.72 V for a current density of  $10 \text{ mA cm}^{-2}$ . The results reveal a promising non-noble catalytic platform for low-cost and high-efficiency H<sub>2</sub> and O<sub>2</sub> production.

## 2 Experimental

### 2.1 Preparation of Co/MoO<sub>2</sub> nanoarrays, Co, and MoO<sub>2</sub>

The carbon cloth (CC) pretreated with ethanol and acetone was soaked overnight in a nitric acid solution to enrich the surface oxygen-containing functional groups. After rinsing with ultrapure water, the CC was dried in a 60 °C oven. 0.1765 g of (NH<sub>4</sub>)<sub>6</sub>Mo<sub>7</sub>O<sub>24</sub>, 0.249 g of Co(CH<sub>3</sub>COO)<sub>2</sub>, 0.12 g of (NH<sub>2</sub>)<sub>2</sub>CO, and 0.185 g of NH<sub>4</sub>F were dissolved in 30 mL of ultrapure water ultrasonically for 30 min, transferred to a 50 mL Teflon-lined stainless autoclave containing the CC, and heated to 150 °C for 6 h. After cooling to room temperature, the CC was taken out, rinsed three times with ultrapure water, and dried in a vacuum freeze-dryer for 12 h. Afterwards, the sample was pyrolyzed at 400 °C for 2 h at a heating rate of  $5 \text{ °C min}^{-1}$  in argon (Ar) and then Ar/H<sub>2</sub> (volume ratio: 90 : 10) at 550 °C for 2 h at a ramping rate of  $5 \text{ °C min}^{-1}$  to form the Co/MoO<sub>2</sub> nanoarrays.

Synthesis of Co proceeded in two steps. The CC was electrodeposited in a 0.1 M cobalt nitrate solution to produce Co(OH)<sub>2</sub> (ref. 20) and then annealed in Ar/H<sub>2</sub> (volume ratio: 90 : 10) at 550 °C for 2 h using a heating rate of  $5 \text{ °C min}^{-1}$ . The pretreated CC was hydrothermally treated to produce MoS<sub>2</sub> and subsequently reacted with air to form MoO<sub>3</sub>.<sup>21</sup> Finally, the MoO<sub>3</sub> sample was collected under Ar/H<sub>2</sub> (90 : 10) at a ramping rate of  $5 \text{ °C min}^{-1}$  to 650 °C for 2 h to form MoO<sub>2</sub> (Fig. S1†).

Pt/C and RuO<sub>2</sub> were fabricated by immersing the  $1 \times 1 \text{ cm}^2$  CC in a uniform Pt/C (or RuO<sub>2</sub>) solution and drying in air. The solution (1 mL) contained isopropanol and ultrapure water (volume ratio of 9 : 1), 1 mg of 20% Pt/C (or RuO<sub>2</sub>), and 20 μL of 5% Nafion were sonicated to obtain a homogeneous solution.

### 2.2 Materials characterization

Field-emission scanning electron microscopy (FE-SEM, Apreo S HiVac) and transmission electron microscopy (TEM, JEM-F200) were performed to examine the microstructure of the materials. X-ray photoelectron spectroscopy (XPS, Axis Supra+) was carried out to determine the chemical states and X-ray diffraction (XRD, Bruker D8A A25) was conducted to investigate the structure.

### 2.3 Electrochemical evaluation

The electrochemical characteristics were determined on the biological VSP300-type electrochemical workstation with the three-electrode setup (Biologic Science Instruments, France) and N<sub>2</sub>-saturated 1 M KOH as the electrolyte. The Co/MoO<sub>2</sub> electrode with a mass loading of  $1 \text{ mg cm}^{-2}$  was the working electrode, carbon rod was the counter electrode, and saturated calomel electrode (SCE) was the reference electrode. The

potentials were standardized as follows based on the reversible hydrogen electrode (RHE):  $E(\text{RHE}) = E(\text{SCE}) + 0.059 \times \text{pH}$  with automatic 85% iR-compensation. Linear sweep voltammetry (LSV) was conducted at a scanning rate of  $5 \text{ mV s}^{-1}$  to obtain the polarization curves to assess the HER performance from  $-1.0675$  to  $-1.5 \text{ V vs. RHE}$ . Similarly, the polarization curves for OER were acquired from 0.8 to 1.8 V vs. RHE. The electrochemically active surface area (ECSA) was determined by cyclic voltammetry (CV) at scanning rates ranging from  $50\text{--}90 \text{ mV s}^{-1}$  and  $-0.6$  to  $-0.8 \text{ V vs. SCE}$ . Electrochemical impedance spectroscopy (EIS) was carried out from 100 kHz to 0.1 Hz with  $0.5 \text{ V vs. SCE}$ . The water splitting electrolyser comprises the bifunctional Co/MoO<sub>2</sub> electrodes and 1 M KOH electrolyte.

## 3 Results and discussion

As shown in Fig. 1, CoMoO<sub>4</sub> nanosheets synthesized on CC hydrothermally are annealed in a reductive Ar/H<sub>2</sub> ambient. The CoMoO<sub>4</sub> nanosheets cover the CC uniformly and the size of the nanosheets are about 10 μm as shown in Fig. 2a. CoMoO<sub>4</sub> is then annealed in Ar/H<sub>2</sub> at 550 °C for 2 h and CoMoO<sub>4</sub> decomposes into Co and MoO<sub>2</sub> composites while maintaining the nanosheet structure of CoMoO<sub>4</sub>. The nanoparticles are evenly dispersed on the surface of nanosheets (Fig. 2b and c). Co/MoO<sub>2</sub> is examined by TEM and Fig. 2d and e disclose that the nanoparticles on the nanosheets are about 20–30 nm in size. The high-resolution TEM (HR-TEM) image (Fig. 2f) reveals distinct lattice fringes with an interplanar distances of 0.21 nm and 0.245 nm corresponding to the (111) and ( $-202$ ) planes of the Co and MoO<sub>2</sub>, respectively.<sup>22,23</sup> The elemental maps of Co/MoO<sub>2</sub> in Fig. 2g corroborate uniform distributions of Co nanoparticles on the MoO<sub>2</sub> nanosheets.

To determine the phase constituents, CoMoO<sub>4</sub> and Co/MoO<sub>2</sub> are analyzed by XRD. Fig. 3a exhibits diffraction peaks at  $25.5^\circ$ ,  $33.7^\circ$ ,  $59.9^\circ$ ,  $61.9^\circ$ , and  $63.1^\circ$  corresponding to CoMoO<sub>4</sub> (JCPDS No. 21-0868) (ref. 21) and new phases of MoO<sub>2</sub> (JCPDS NO. 78-1070) (ref. 22) and metallic cobalt (JCPDS No. 15-0806) (ref. 23) are formed after reduction at 550 °C for 2 h in Ar/H<sub>2</sub>. The results demonstrate that the CoMoO<sub>4</sub> precursor is reduced in Ar/H<sub>2</sub> to generate Co and MoO<sub>2</sub>.

The change in the chemical states after phase separation is monitored by X-ray photoelectron spectroscopy (XPS). As shown in Fig. 3b, Co/MoO<sub>2</sub> exhibits peaks of Co, Mo, O, and C. The fine spectrum of Co 2p of CoMoO<sub>4</sub> in Fig. 3c can be fitted with peaks at 781.3 (Co<sup>2+</sup> 2p<sub>3/2</sub>), 797.2 (Co<sup>2+</sup> 2p<sub>1/2</sub>), 785.1, and 802.8 eV corresponding to the cobalt oxide Co<sup>(II)</sup> and satellite peaks,<sup>24</sup> respectively. The metallic Co peaks of Co/MoO<sub>2</sub> at 778.5 eV (Co<sup>0</sup> 2p<sub>3/2</sub>) and 793.5 eV (Co<sup>0</sup> 2p<sub>1/2</sub>)<sup>25</sup> confirm that cobalt is formed in

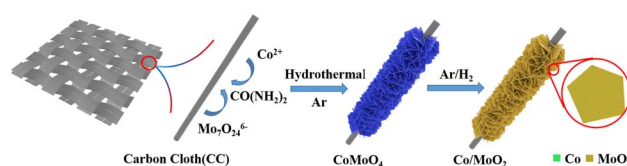


Fig. 1 Schematic illustration of the fabrication of Co/MoO<sub>2</sub>.



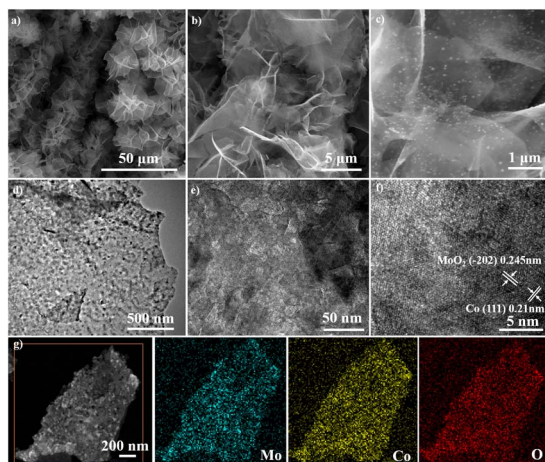


Fig. 2 FE-SEM images of (a)  $\text{CoMoO}_4$  and (b and c)  $\text{Co}/\text{MoO}_2$ , (d–f) TEM image of  $\text{Co}/\text{MoO}_2$ , and (g) elemental maps of  $\text{Co}/\text{MoO}_2$ .

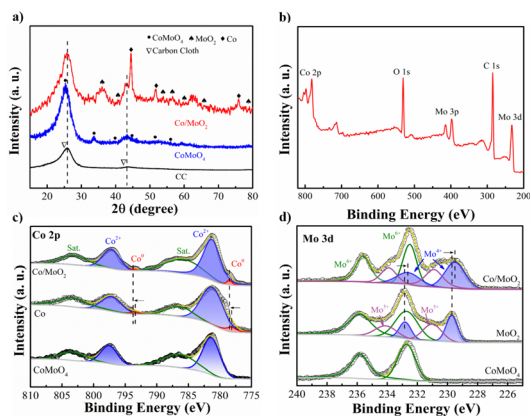


Fig. 3 (a) XRD patterns of CC,  $\text{CoMoO}_4$  and  $\text{Co}/\text{MoO}_2$ , (b) XPS spectrum of  $\text{Co}/\text{MoO}_2$ , and high-resolution XPS spectra of (c) Co 2p and (d) Mo 3d of  $\text{CoMoO}_4$ ,  $\text{Co}/\text{MoO}_2$ ,  $\text{MoO}_2$  and Co.

the phase separation process. It can be seen that the Co 2p spectra of  $\text{Co}/\text{MoO}_2$  varied to a higher binding energy than Co, manifesting the electrons depletion region on the sample of Co. Fig. 3d shows two peaks at 232.6 eV and 235.8 eV in the Mo 3d XPS spectrum associated with Mo  $3d_{5/2}$  and Mo  $3d_{3/2}$  of the  $\text{Mo}^{6+}$  state of  $\text{CoMoO}_4$ .<sup>26</sup> With regard to the reduced sample, the peaks at 229.5, 232.6, 230.8, 233.8, 232.5, and 235.5 eV are ascribed to the intermediate states of  $\text{Mo}^{4+}$ ,  $\text{Mo}^{5+}$  and  $\text{Mo}^{6+}$ , further confirming the formation of  $\text{MoO}_2$ .<sup>27–31</sup> As shown in the graph, the Mo 3d spectra of  $\text{Co}/\text{MoO}_2$  transferred to a lower binding energy as contrasted with the sample of  $\text{MoO}_2$ , which demonstrate the electrons accumulation on the  $\text{MoO}_2$ . Thus, the electrons transfer from Co to  $\text{MoO}_2$ .

The electrocatalytic OER and HER characteristics are determined by LSV at a scan rate of  $5 \text{ mV s}^{-1}$  using a three-electrode configuration in  $\text{N}_2$ -saturated 1 M KOH. A low overpotential ( $\eta$ ) and small Tafel slope reflect high electrocatalytic activity in OER and HER at the desired large current density. For comparison Co,  $\text{MoO}_2$ ,  $\text{RuO}_2$  and Pt/C catalysts are also studied. Fig. 4a and c

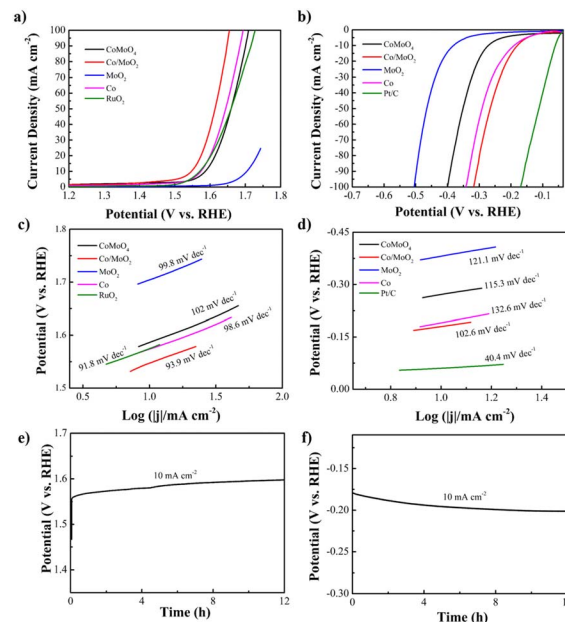


Fig. 4 (a) OER polarization curves of  $\text{CoMoO}_4$ ,  $\text{Co}/\text{MoO}_2$ ,  $\text{MoO}_2$ , Co, and  $\text{RuO}_2$ , (b) HER polarization curves of  $\text{CoMoO}_4$ ,  $\text{Co}/\text{MoO}_2$ ,  $\text{MoO}_2$ , Co, and 20% Pt/C, (c) Tafel plots for OER, (d) Tafel plots for HER, (e)  $\text{Co}/\text{MoO}_2$  galvanostatic results for OER, and (f)  $\text{Co}/\text{MoO}_2$  galvanostatic results for HER.

present the OER polarization and corresponding Tafel plots of the samples. The OER overpotential ( $\eta_{10}$ ) of  $\text{Co}/\text{MoO}_2$  is 318 mV, which is better than those of  $\text{CoMoO}_4$  (355 mV),  $\text{RuO}_2$  (345 mV), Co (343 mV) and  $\text{MoO}_2$  (470 mV). It is due to better electron transfer from Co to  $\text{MoO}_2$  at the  $\text{Co}/\text{MoO}_2$  interface consequently enriching the positive charges on the Co surface and simultaneously reducing the adsorption capacity of Co particles to oxygen species at the interface, resulting in enhanced oxygen evolution activity.<sup>32</sup> Therefore, the  $\text{Co}/\text{MoO}_2$  composite is beneficial to the interfacial structure to enhance the intrinsic activity. Co and  $\text{MoO}_2$  promote oxygen evolution in alkaline solutions. Moreover,  $\eta_{10}$  of  $\text{Co}/\text{MoO}_2$  is better than those of previously reported catalysts such as  $\text{MoO}_2/\text{NF}$  (350 mV),<sup>33</sup>  $\text{MoO}_2+\text{OH}^-$  (435 mV),<sup>34</sup>  $\text{MoO}_2\text{-Co}$  (378 mV),<sup>35</sup>  $\text{MoO}_2\text{-Co}_2\text{Mo}_3\text{-O}_8@\text{C}$  (320 mV),<sup>36</sup>  $\text{Co}_2\text{N}_{0.67}\text{-BHP}$  (340 mV),<sup>37</sup>  $\text{Co}/\beta\text{-MoO}_2\text{-C@N-CNTs}$  (356 mV)<sup>38</sup> (Table S1†). The corresponding Tafel slope of  $\text{Co}/\text{MoO}_2$  is  $93.9 \text{ mV dec}^{-1}$ , which is smaller than those of  $\text{CoMoO}_4$  ( $102 \text{ mV dec}^{-1}$ ), Co ( $98.6 \text{ mV dec}^{-1}$ ), and  $\text{MoO}_2$  ( $99.8 \text{ mV dec}^{-1}$ ). Hence,  $\text{Co}/\text{MoO}_2$  has a smaller  $\eta_{10}$  and Tafel slope on account of the synergistic effects rendered by the individual heterostructures such as rapid desorption of gas and maintenance of active sites during gas generation.<sup>13</sup> Electron transfer between Co and  $\text{MoO}_2$  enhances the electron donating ability and the bonding force between the transition metal Co and  $\text{OH}^-$  increases to improve the OER performance.<sup>29</sup> In addition, metallic cobalt enhances the oxygen evolution kinetics of  $\text{Co}/\text{MoO}_2$  by promoting the conductivity and accelerating transfer of electrons. Therefore,  $\text{Co}/\text{MoO}_2$  prepared by phase separation boosts the oxygen evolution capability.





The electrocatalytic HER properties are determined by LSV is shown in Fig. 4b and d. Co/MoO<sub>2</sub> shows a smaller  $\eta_{10}$  of 178 mV compared to CoMoO<sub>4</sub> (272 mV), Co (192 mV), and MoO<sub>2</sub> (380 mV). For comparison, the Pt/C catalyst has a  $\eta_{10}$  of 59 mV in 1 M KOH. The HER properties of Co/MoO<sub>2</sub> are better than of recently reported catalysts including MoO<sub>2</sub> (200 mV),<sup>39</sup> MoO<sub>2</sub>/NF (187 mV),<sup>33</sup> Co@ $\beta$ -Mo<sub>2</sub>C-NC-0.115 (188 mV),<sup>40</sup> MoO<sub>2</sub>-Co (422 mV),<sup>35</sup> Co-CoO/BC (210 mV),<sup>41</sup> Mo<sub>2</sub>C/MoO<sub>2</sub> (204 mV)<sup>42</sup> (Table S2†). The HER reaction involves two stages.<sup>43</sup> The first steep is the Volmer reaction with a Tafel slope of about 118 mV dec<sup>-1</sup> and the second one is the Heyrovsky reaction with a Tafel slope of approximately 39 mV dec<sup>-1</sup> or Tafel reaction with a Tafel slope of 29 mV dec<sup>-1</sup>. The HER Tafel slope of Co/MoO<sub>2</sub> is 102.6 mV dec<sup>-1</sup> indicative of the Volmer-Heyrovsky mechanism. The hydrogen evolution reaction requires a large number of protons which in an alkaline solution originate from dissociation of water. Therefore, the hydrogen evolution rate of Co/MoO<sub>2</sub> in the alkaline solution is governed by the Volmer reaction. The Tafel slope of Co/MoO<sub>2</sub> is smaller than those of CoMoO<sub>4</sub> (115.3 mV dec<sup>-1</sup>), Co (132.6 mV dec<sup>-1</sup>), and MoO<sub>2</sub> (121.1 mV dec<sup>-1</sup>). Metallic cobalt provides the H\* adsorption sites to promote water dissociation and improving the Co/MoO<sub>2</sub> HER properties.<sup>44</sup> Furthermore, Mo-H has a strong adsorption energy which inhibits desorption. The electronic structure of Mo is regulated by the transition metal Co, which diminishes the Mo-H binding energy and makes it easier to desorb. Consequently, hydrogen evolution from Co/MoO<sub>2</sub> is further improved.<sup>13</sup> When Co/MoO<sub>2</sub> transfers electrons from Co to MoO<sub>2</sub>, the Co surface is enriched with positive charges and the Co particles near the interface decreases the ability to adsorb hydrogen to enhance hydrogen evolution.<sup>45</sup> Therefore, the Co/MoO<sub>2</sub> heterojunction improves the intrinsic activity of Co and MoO<sub>2</sub> synergistically in the alkaline solution. Galvanostatic tests are performed on the Co/MoO<sub>2</sub> catalyst for both OER and HER as shown in Fig. 4e and f further revealing the stability in the electrochemical reaction.

The electrochemical active surface area (ECSA) is another critical parameter for the catalytic activity and characterized by the electrochemical double layer capacitance ( $C_{dl}$ ). Cyclic voltammetry (CV) is performed at different scanning rates in the non-Faraday current interval (Fig. S2†). The electric double layer capacitance is related to the number of active sites in the electrochemical reaction<sup>46</sup> and CV is utilized to determine the number of active sites. As shown in Fig. 5a, the  $C_{dl}$  value of Co/MoO<sub>2</sub> (23.2 mF cm<sup>-2</sup>) is bigger than those of MoO<sub>2</sub> (3.4 mF cm<sup>-2</sup>) and Co (5.8 mF cm<sup>-2</sup>), implying that the Co/MoO<sub>2</sub> catalyst has more active sites. Electrochemical impedance spectroscopy (EIS) is employed to study the interfacial dynamics and as shown in the equivalent series model composed of the solution resistance  $R_s$  (intersection between the high frequency region and X-axis), CPE (constant phase angle element), and parallel  $R_{ct}$ , the faster charge transfer and transmission, the smaller is the diameter of the semi-circular  $R_{ct}$ . Fig. 5b shows smaller  $R_{ct}$  than others (Fig. S3†) because that *in situ* formation of Co/MoO<sub>2</sub> reduces the interface resistance and raises the charge conduction rate thus exploiting the synergetic effects rendered by Co and MoO<sub>2</sub>. The calculated differential charge

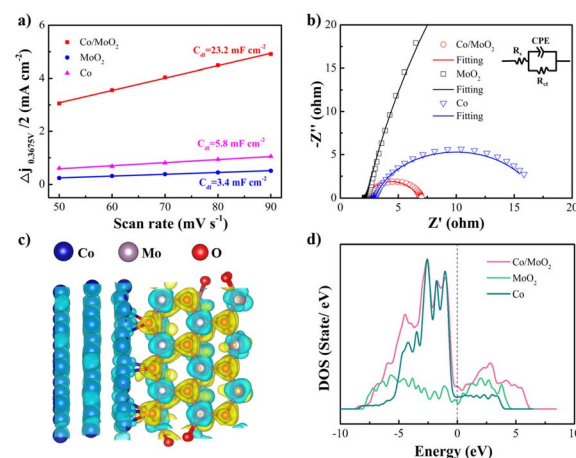


Fig. 5 (a) Current densities ( $\Delta j = j_{anode} - j_{cathode}$ , at 0.36 V) as a function of scanning rates of Co/MoO<sub>2</sub>, MoO<sub>2</sub> and Co with the corresponding slope being twice that of  $C_{dl}$ , (b) Nyquist plots collected at 500 mV vs. SCE of Co/MoO<sub>2</sub>, MoO<sub>2</sub> and Co, (c) differential charge densities of Co/MoO<sub>2</sub>, and (d) density of states of Co/MoO<sub>2</sub>, MoO<sub>2</sub> and Co.

density in Fig. 5c illustrates that the charge density redistributes at the interface showing an electron accumulation region (yellow region) on the MoO<sub>2</sub> side and electron loss region (blue region) on the Co side, indicating electron transfer from Co to MoO<sub>2</sub>. The density of states (DOS) in Fig. 5d reveals that the state of Co/MoO<sub>2</sub> is located at the Fermi level higher than MoO<sub>2</sub> and Co, thereby explaining why Co/MoO<sub>2</sub> improves the electron activity as consistent with the Fig. 5b.

Co/MoO<sub>2</sub> catalysts are prepared at different temperature and the HER and OER characteristics are evaluated by LSV to assess the influence of the catalyst configuration and composition on the electrochemical properties (Fig. S4†). Owing to the proper structure, Co/MoO<sub>2</sub> prepared at 550 °C delivers better electrocatalytic performance than other samples. As shown in Fig. S5 and S6,† when the temperature is 450 °C, the nanosheets are still CoMoO<sub>4</sub> and no particles are deposited on the nanosheets. However, at 650 °C, the morphology changes into a porous network because of the formation of the new phase of Co<sub>3</sub>Mo (JCPDS NO. 29-0488).<sup>13</sup>

The Co/MoO<sub>2</sub> catalysts are assembled as the anode and cathode to conduct overall water splitting in 1 M KOH. The cell

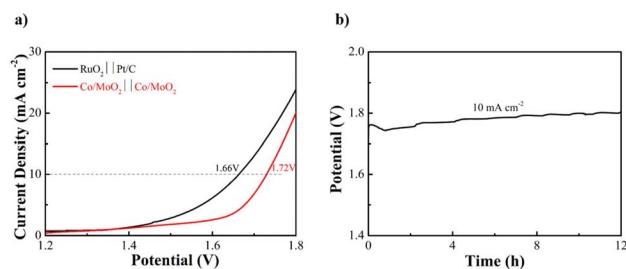


Fig. 6 (a) Water splitting LSV curves of Co/MoO<sub>2</sub> as both the cathode and anode and (b) Co/MoO<sub>2</sub> water splitting electrolyzer galvanostatic test for 12 h at 10 mA cm<sup>-2</sup>.

voltage is 1.72 V at a current density of 10 mA cm<sup>-2</sup>, which is competitive to the other non-noble metal bifunctional catalysts reported in the literature, including Co@β-Mo<sub>2</sub>C-NC-0.115 (1.72 V),<sup>40</sup> Co<sub>2</sub>P/Mo<sub>2</sub>C/Mo<sub>3</sub>Co<sub>3</sub>C@C (1.74 V),<sup>47</sup> Co-CoO/BC (1.77 V),<sup>41</sup> P-MoO<sub>2</sub> (1.83 V),<sup>48</sup> NiO/NiFe<sub>2</sub>O<sub>4</sub> (1.82 V)<sup>49</sup> (Table S3†). The overall water splitting potential of the Co/MoO<sub>2</sub>-based electrolyzer rises slightly after continuous operation for 12 h in the alkaline solution (Fig. 6).

## 4 Conclusions

A Co/MoO<sub>2</sub> catalyst is fabricated by a one-step phase separation process of CoMoO<sub>4</sub> in the Ar/H<sub>2</sub> atmosphere. The *in situ* generated metallic Co nanoparticles on the MoO<sub>2</sub> nanosheets improve the HER characteristics of MoO<sub>2</sub>, whereas the MoO<sub>2</sub> nanosheets impede agglomeration of nanosized Co in OER. The Co/MoO<sub>2</sub> composite shows superior HER and OER properties compared to single-phase catalysts of Co and MoO<sub>2</sub>. In the alkaline solution, the  $\eta_{10}$  values of Co/MoO<sub>2</sub> for HER and OER are 178 and 318 mV, respectively. The electrolytic cell assembled with the bifunctional Co/MoO<sub>2</sub> electrocatalyst shows a low voltage of 1.72 V for a current density of 10 mA cm<sup>-2</sup> in overall water splitting. The *in situ* separation strategy to form the transition metal and oxide heterojunction has large potential in designing non-noble metal catalysts for electrocatalytic water splitting and other applications.

## Author contributions

LX implemented the experiment, analyzed the data and wrote the article. YL, HS, XL, WG, XJ, MJ and XZ participated in the formulation of the experimental scheme. BG and PC revised the article.

## Conflicts of interest

There are no conflicts to declare.

## Acknowledgements

This work was financially supported by the College Student Innovation and Entrepreneurship Training Program of Hubei Province (S202110488013), Hubei Key Laboratory for Efficient Utilization and Agglomeration of Metallurgic Mineral Resources Open Project Fund (2019zy004), Foundation of Science Research Program from the Hubei Provincial Department of Education (No. Q20221101), Hubei Province Natural Science Foundation Innovation Group Project (2019CFA020), Young Top-notch Talent Cultivation Program of Hubei Province and Outstanding Youth Foundation of Natural Science Foundation of Hubei Province (2020CFA099), City University of Hong Kong Donation Research Grant (DON-RMG 9229021), City University of Hong Kong Donation Grant (9220061), Hong Kong ITC (Innovation and Technology Commission) ITF (Innovation and Technology Fund) (GHP/149/20SZ and CityU 9440296), as well as Shenzhen-Hong Kong Innovative Collaborative Research and Development Program (SGLH20181109110802117 and

CityU 9240014). Thank the Analysis and Testing Center of Wuhan University of Science and Technology for analytical support.

## Notes and references

- W. J. Jiang, T. Tang, Y. Zhang and J. S. Hu, *Acc. Chem. Res.*, 2020, **53**, 1111–1123.
- Z. Zheng, L. Yu, M. Gao, X. Chen, W. Zhou, C. Ma, L. Wu, J. Zhu, X. Meng, J. Hu, Y. Tu, S. Wu, J. Mao, Z. Tian and D. Deng, *Nat. Commun.*, 2020, **11**, 3315.
- Y. Chen, Y. Wang, J. Yu, G. Xiong, H. Niu, Y. Li, D. Sun, X. Zhang, H. Liu and W. Zhou, *Adv. Sci.*, 2022, **9**, 2105869.
- X. Zou and Y. Zhang, *Chem. Soc. Rev.*, 2015, **44**, 5148–5180.
- N. T. Suen, S. F. Hung, Q. Quan, N. Zhang, Y. J. Xu and H. M. Chen, *Chem. Soc. Rev.*, 2017, **46**, 337–365.
- B. Chang, J. Yang, Y. Shao, L. Zhang, W. Fan, B. Huang, Y. Wu and X. Hao, *ChemSusChem*, 2018, **11**, 3198–3207.
- X. Xie, L. Lin, R. Y. Liu, Y. F. Jiang, Q. Zhu and A. W. Xu, *J. Mater. Chem. A*, 2015, **3**, 8055–8061.
- J. Guo, J. Wang, Z. Wu, W. Lei, J. Zhu, K. Xia and D. Wang, *J. Mater. Chem. A*, 2017, **5**, 4879–4885.
- L. Wu, X. Wang, Y. Sun, Y. Liu and J. Li, *Nanoscale*, 2015, **7**, 7040–7044.
- Y. Jin, H. Wang, J. Li, X. Yue, Y. Han, P. K. Shen and Y. Cui, *Adv. Mater.*, 2016, **28**, 3785–3790.
- Y. Jin and P. K. Shen, *J. Mater. Chem. A*, 2015, **3**, 20080–20085.
- X. Zhang, F. Zhou, W. Pan, Y. Liang and R. Wang, *Adv. Funct. Mater.*, 2018, **28**, 1804600.
- J. Chen, Y. Ge, Q. Feng, P. Zhuang, H. Chu, Y. Cao, W. R. Smith, P. Dong, M. Ye and J. Shen, *ACS Appl. Mater. Interfaces*, 2019, **11**, 9002–9010.
- Z. Chen, X. Duan, W. Wei, S. Wang and B. J. Ni, *J. Mater. Chem. A*, 2019, **7**, 14971–15005.
- X. Yan, L. Tian, S. Atkins, Y. Liu, J. Murowchick and X. B. Chen, *ACS Sustainable Chem. Eng.*, 2016, **7**, 3743–3749.
- M. Gong, W. Zhou, M. C. Tsai, J. Zhou, M. Guan, M. C. Lin, B. Zhang, Y. Hu, D. Y. Wang, J. Yang, S. J. Pennycook, B. J. Hwang and H. Dai, *Nat. Commun.*, 2014, **5**, 4695.
- G. Liu, H. Bai, Y. Ji, L. Wang, Y. Wen, H. Lin, L. Zheng, Y. Li, B. Zhang and H. Peng, *J. Mater. Chem. A*, 2019, **7**, 12434–12439.
- X. Liu, K. Ni, C. Niu, R. Guo, W. Xi, Z. Wang, J. Meng, J. Li, Y. Zhu, P. Wu, Q. Li, J. Luo, X. Wu and L. Mai, *ACS Catal.*, 2019, **9**, 2275–2285.
- H. Zhao, Z. Li, X. Dai, M. Cui, F. Nie, X. Zhang, Z. Ren, Z. Yang, Y. Gan, X. Yin, Y. Wang and W. Song, *J. Mater. Chem. A*, 2020, **8**, 6732–6739.
- X. Yang, A. Y. Lu, Y. Zhu, M. N. Hedhili, S. Min, K. W. Huang, Y. Han and L. J. Li, *Nano Energy*, 2015, **15**, 634–641.
- K. Wu, J. Zhan, G. Xu, C. Zhang, D. Pan and M. Wu, *Nanoscale*, 2018, **10**, 16040–16049.
- X. F. Lu, Y. Chen, S. Wang, S. Gao and X. W. Lou, *Adv. Mater.*, 2019, **31**, 1902339.
- L. X. Song, M. Wang, S. Z. Pan, J. Yang, J. Chen and J. Yang, *J. Mater. Chem.*, 2011, **21**, 7982–7989.



- 24 J. Jiang, Q. Liu, C. Zeng and L. Ai, *J. Mater. Chem. A*, 2017, **5**, 16929–16935.
- 25 X. Lang, M. A. Qadeer, G. Shen, R. Zhang, S. Yang, J. An, L. Pan and J. J. Zou, *J. Mater. Chem. A*, 2019, **7**, 20579–20583.
- 26 H. Jiang, Z. Cui, C. Xu and W. Li, *Chem. Commun.*, 2019, **55**, 9432–9435.
- 27 X. Shi, A. Wu, H. Yan, L. Zhang, C. Tian, L. Wang and H. Fu, *J. Mater. Chem. A*, 2018, **6**, 20100–20109.
- 28 Y. Lu, H. Ang, Q. Yan and E. Fong, *Chem. Mater.*, 2016, **28**, 5743–5752.
- 29 N. K. Oh, C. Kim, J. Lee, O. Kwon, Y. Choi, G. Y. Jung, H. Y. Lim, S. K. Kwak, G. Kim and H. Park, *Nat. Commun.*, 2019, **10**, 1723.
- 30 C. Li, H. Jang, M. G. Kim, L. Hou, X. Liu and J. Cho, *Appl. Catal., B*, 2022, **307**, 121204.
- 31 H. Guo, A. Wu, Y. Xie, H. Yan, D. Wang, L. Wang and C. Tian, *J. Mater. Chem. A*, 2021, **9**, 8620–8629.
- 32 C. Liu, K. Wang, X. Zheng, X. Liu, Q. Liang and Z. Chen, *Carbon*, 2018, **139**, 1–9.
- 33 Y. Sun, Y. Zhou, Y. Zhu, Y. Shen and A. Xie, *ACS Sustainable Chem. Eng.*, 2019, **7**, 9153–9163.
- 34 P. Guha, B. Mohanty, R. Thapa, R. M. Kadam, P. V. Satyam and B. K. Jena, *ACS Appl. Energy Mater.*, 2020, **3**, 5208–5218.
- 35 Y. Li, C. Wang, M. Cui, J. Xiong, L. Mi and S. Chen, *Appl. Surf. Sci.*, 2021, **543**, 148804.
- 36 Y. Li, H. Xu, H. Huang, C. Wang, L. Gao and T. Ma, *Chem. Commun.*, 2018, **54**, 2739–2742.
- 37 X. Lv, Z. Xiao, H. Wang, X. Wang, L. Shan, F. Wang, C. Wei, X. Tang and Y. Chen, *J. Energy Chem.*, 2021, **54**, 626–638.
- 38 T. Ouyang, Y.-Q. Ye, C.-Y. Wu, K. Xiao and Z.-Q. Liu, *Angew. Chem., Int. Ed.*, 2019, **58**, 4923–4928.
- 39 B. Wang, Z. Zhang, S. Zhang, Y. Cao, Y. Su, S. Liu, W. Tang, J. Yu, Y. Ou, S. Xie, J. Li and M. Ma, *Electrochim. Acta*, 2020, **359**, 136929.
- 40 U. Ali, Y. Yu, J. Guo, Y. Liu, Z. Mu and S. Xing, *J. Electrochem. Soc.*, 2020, **167**, 044520.
- 41 M. Yang, D. Wu and D. Cheng, *Int. J. Hydrogen Energy*, 2019, **44**, 6525–6534.
- 42 M. Liu, Y. Yang, X. Luan, X. Dai, X. Zhang, J. Yong, H. Qiao, H. Zhao, W. Song and X. Huang, *ACS Sustainable Chem. Eng.*, 2018, **6**, 14356–14364.
- 43 Y. Shi and B. Zhang, *Chem. Soc. Rev.*, 2016, **45**, 1529–1541.
- 44 G. Cai, W. Zhang, L. Jiao, S. H. Yu and H. L. Jiang, *Chem*, 2017, **2**, 791–802.
- 45 X. Yan, L. Tian, M. He and X. Chen, *Nano Lett.*, 2015, **15**, 6015–6021.
- 46 Z. H. Deng, L. Li, W. Ding, K. Xiong and Z. D. Wei, *Chem. Commun.*, 2015, **51**, 1893–1896.
- 47 X. Li, X. Wang, J. Zhou, L. Han, C. Sun, Q. Wang and Z. Su, *J. Mater. Chem. A*, 2018, **6**, 5789–5796.
- 48 Z. Cui, T. Feng, X. Wang, P. Guo, W. Wang, M. E. Yue and Z. Li, *Fuel*, 2023, **332**, 126250.
- 49 H. Zhong, G. Gao, X. Wang, H. Wu, S. Shen, W. Zuo, G. Cai, G. Wei, Y. Shi, D. Fu, C. Jiang, L. W. Wang and F. Ren, *Small*, 2021, **17**, 2103501.

